CHAPTER 5

MICROSTRUCTURAL, MECHANICAL, AND WEAR BEHAVIOUR OF A 319 ALLOY CAST IN A DIFFERENT MOLD

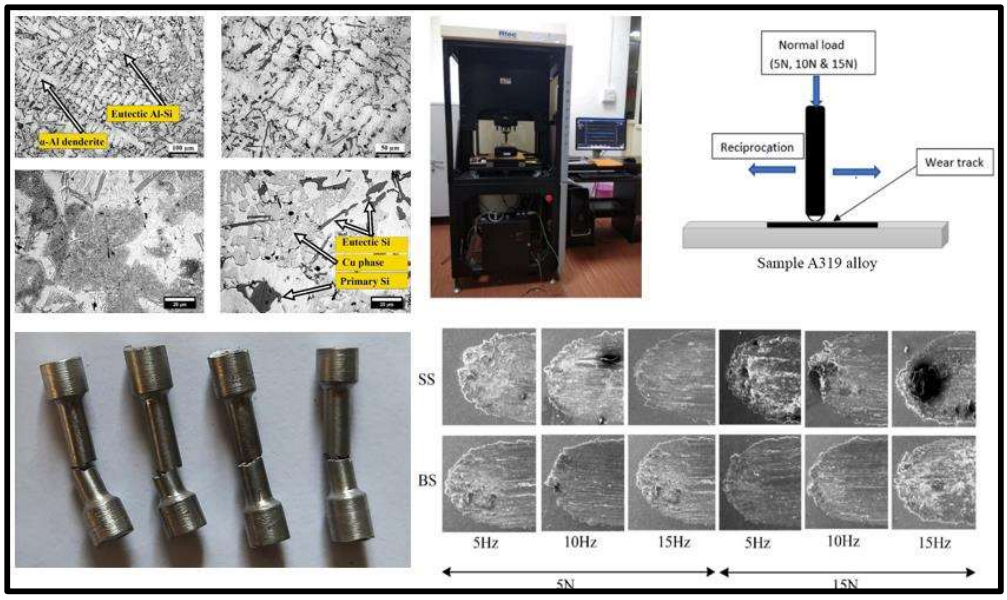

5.1 INTRODUCTION

This chapter is primarily concerned with the casting of A319 alloy in sand-slag mold and sand mold. In terms of microstructural characteristics, mechanical characteristics, and tribological behaviour, the performance of the as-cast alloy has been discussed. Alterations in the morphology of the microstructure, mechanical properties, and tribological behaviour can be affected by the secondary dendritic arm spacing (SDAS). To determine the viability of a sand-slag mold, it is necessary to take into account the changes in the secondary dendritic arm spacing of the alloy cast in various molds. Due to this, the chapter has been separated into three sections: I. Microstructural analysis; II. Mechanical characteristics; and III. Tribological behaviour.

5.2 CHARACTERIZATION

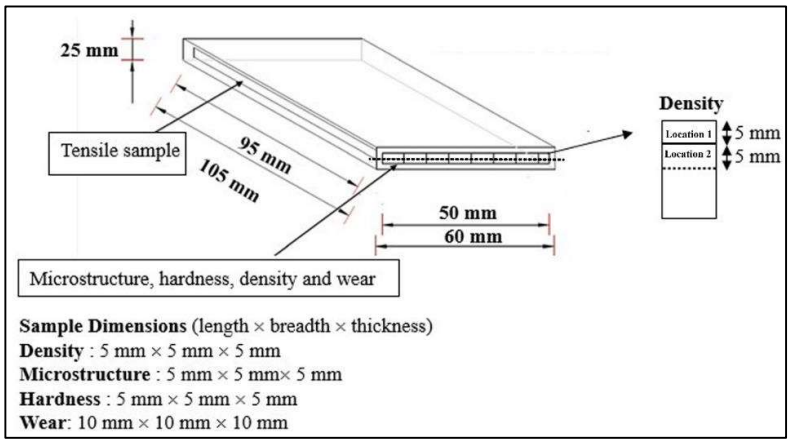

Figure 5.1: Schematic view of the Test Sample

Figure 5.1 shows the location of the sample extracted for the execution of various tests such as density, microstructure, hardness, tensile, and wear with sample dimensions.

5.2.1 Microstructural Analysis

According to standard metallographic procedure (ASTM E3-11), the samples were prepared through grinding (grit of SiC emery papers used in the range of 500-2500), mechanical polishing (with diamond paste), and chemical etching with freshly prepared

Keller reagent (distilled water (190 ml), nitric acid (5 ml), hydrochloric acid (3 ml), and hydrofluoric acid (2 ml)) for the microstructure. The secondary dendritic arm spacing was determined using ImageJ software after being examined under an optical microscope (LEICA - 295).

5.2.2 Secondary dendritic arm spacing (SDAS)

The microstructure with a magnification of 200µm was used for the computation of the secondary dendritic arm spacing (SDAS) using ImageJ software. The SDAS measurements were made parallel to the primary dendrites, between two successive secondary arms, as seen in figure 5.2. The equation (5.1) was used to determine SDAS by counting the secondary dendrites along the primary dendrite [20,184,185].

$$SDAS = \frac{L_p}{n_s - 1} \tag{5.1}$$

Where;

L_p: Distance between first to last secondary dendrite arm

n_s: number of secondary dendritic arms

The average SDAS was determined using a minimum10 number of primary dendrites having secondary dendritic arms of microstructure with a magnification of 200µm.

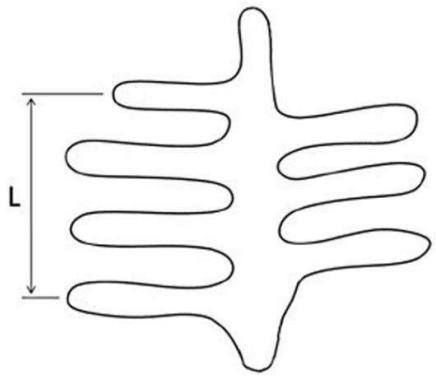

Figure 5.2: Secondary dendritic arm spacing

5.2.3 Density/ Porosity

The Archimedes principle, a hydrostatic displacement technique that compares sample masses in air and water, was used to determine density. Density is determined by the following equation (5.2). [186–189].

$$\rho = \frac{m_a}{m_a - m_w} \tag{5.2}$$

Where;

m_a: mass of the sample in the air (gm); m_w: Mass of the sample in water(gm). Theoretical density was measured based on the rule of the mixture as equation (5.3):

$$\frac{100}{\rho_{th}} = \frac{w_1}{\rho_{Al}} + \frac{w_2}{\rho_{si}} + \frac{w_3}{\rho_{Cu}} + \ldots\ldots\ldots = \sum wi/\rho i \tag{5.3}$$

Where;

Wi: weight % of the constituent element in A319 alloy,

ρi: density of a constituent element

Based on experimental and theoretical density, the porosity of the casting was measured according to equation (5.4) as followed:

$$Porosity = \frac{\rho_{th} - \rho_{ac}}{\rho_{th}} \times 100 \tag{5.4}$$

Where; ρ_{th}: theoretical density, ρ_{ac}: actual density.

5.2.4 Tensile strength

The Instron Universal testing device was used to evaluate the ultimate tensile strength (U.T.S), yield strength (Y.S), and percent elongation (% EL) of the sample, the sample was prepared following ASTM E8 standard and is depicted in figure 5.3. Three

samples were taken for each cast condition to determine the average value of Y.S, U.T.S, and% EL.

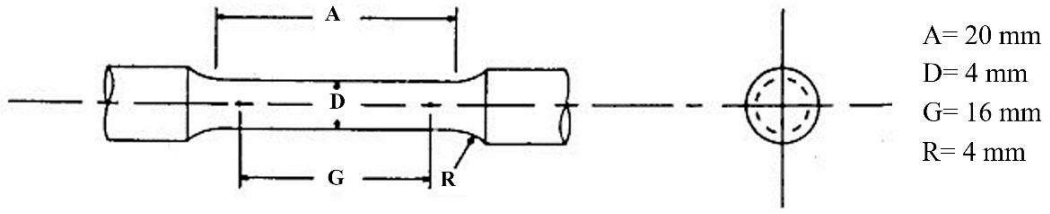

Figure 5.3: Tensile sample

5.2.5 Hardness

Vickers microhardness tester (Model- MINI FLEX 600 DETEX ULTRA, Japan) was used for the microhardness test. Before conducting the test, samples were polished carefully so that the diamond-shaped indentation can be visualized in the microscope enclosed with the machine. 1 kgf Load with 10 sec dwell time was used for the hardness investigation of a cast sample. The average hardness value was counted with 5 readings per sample at a different location.

5.2.6 Wear

i. *Preparation of wear sample*

A square sample of 10 mm × 10 mm was prepared as shown in figure 5.4. The wear sample was polished using silicon carbide emery paper of different numbers such as 500, 1000 and 2500, after polishing on the emery paper cloth polishing was also done to achieve a Ra value of 0.1 ± 0.05. The steel ball was used according to the ASTM G133 standard for the reciprocating ball on the disc wear test. Three tests of similar parameters were repeated on the same sample at a different position to ensure the standard deviation during the test.

$$\boldsymbol{Wear\ rate} = \frac{\boldsymbol{weight\ loss}}{\boldsymbol{Distance\ travel}} \qquad (5.5)$$

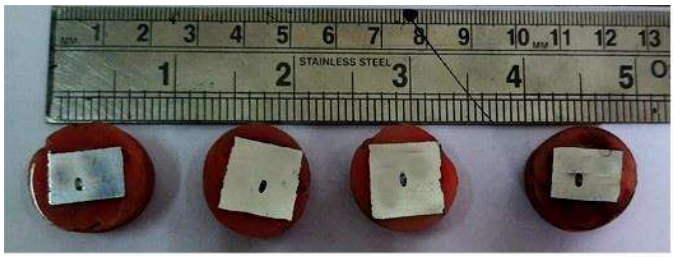

Figure 5.4: Sample of wear test

ii. *Wear test condition*

Reciprocating wear was conducted under ambient conditions having a relative humidity of 45-55%, with the variation in the normal load (5 N, 10 N and15 N) and frequency (5 Hz, 10 Hz, and 15 Hz) for 20 minutes on Multi-Functional Tribometer (Rtech instrument, USA) as shown in figure 5.5 & 5.6 as per ASTMG133. The steel ball (ϕ 6 mm) of AISI 52100 was held against the sample. The sample was mounted on a reciprocating bench, which was reciprocated at an average speed of 0.02 m/s, and wear track length of 2 mm, and each test was conducted for 20 min. A weight balance (0.0001g accuracy) was used to measure the weight of the sample before and after the test. Weight loss was measured to estimate the wear rate. The wear rate was calculated as weight loss per unit of sliding distance (mg/km) as per equation 5.5. Contact pressure due to the ball (spherical) pressed on the flat specimen (plane) was governed through equations (5.6 & 5.7)[190].

$$a = \sqrt[3]{\frac{3F}{8}\frac{\frac{(1-v_1^2)}{E_1}+\frac{(1-v_2{}^2)}{E_2}}{\frac{1}{d_1}+\frac{1}{d_2}}} \tag{5.6}$$

$$P_{max} = \frac{3F}{2\pi a^2} \tag{5.7}$$

Where;

a= Area of contact, P= Maximum contact pressure, v_1 and v_2= Poisson ratio of sample and ball, E_1 and E_2= Elastic modulus of sample and ball, d_1 and d_2 = Diameter of a sample ($d_1 \rightarrow \infty$) and ball

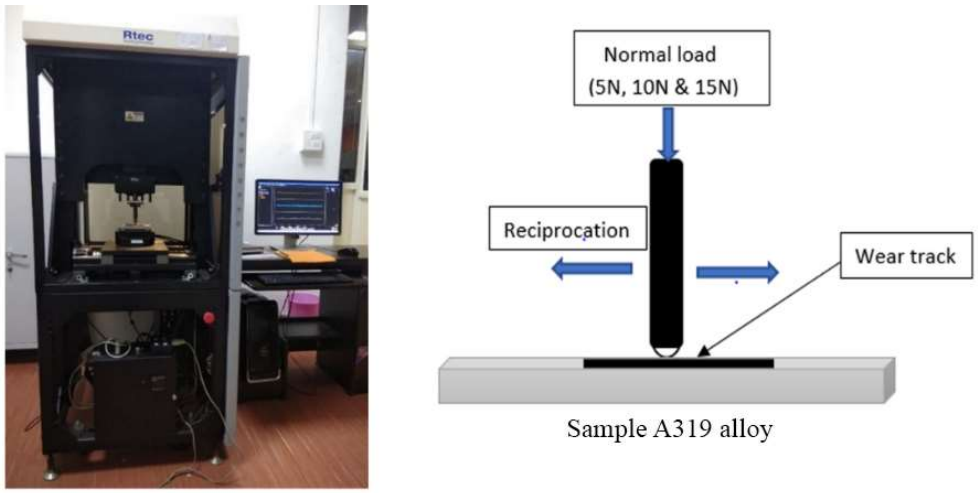

Figure 5.5: Wear test machine universal tribometer and Schematic view of reciprocating wear

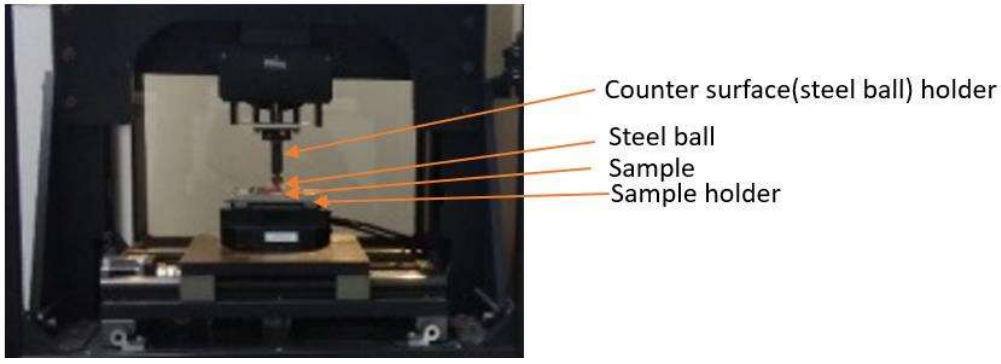

Figure 5.6: Position of sample and steel ball

5.3 RESULTS

5.3.1 Microstructure

Figure 5.7 depicts the microstructure of A319 alloy cast in SS mold. The microstructure mainly consists of a white α- Al dendrites network, dark grey silicon particles, eutectic Al-Si segregated into the inter-dendritic region, Cu phase, etc as shown in figure 5.5. The presence of the Cu phase and Al-Fe-Si was also confirmed through XRD analysis as shown in figure 5.8. In the casting, nucleation of grain takes place at the mold/metal interface. However, the undercooling facilitated a large number of nuclei formation at the mold/ metal interface which result in a fine microstructure.

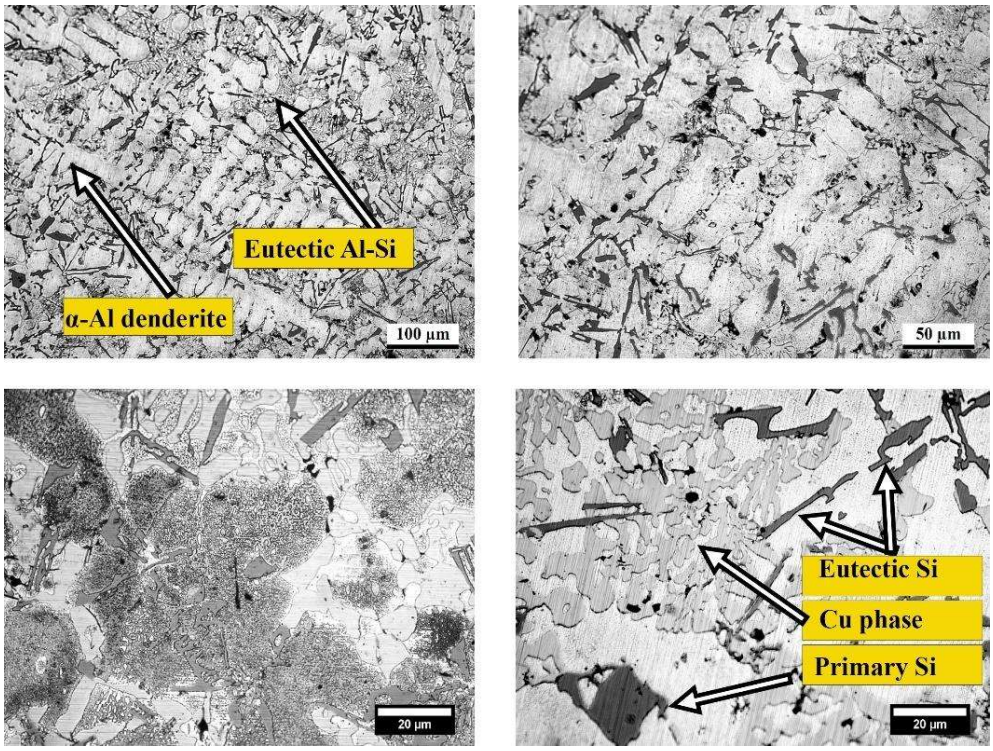

Figure 5.7: Microstructure of A319 alloy cast in a sand mold

The nuclei are randomly oriented and grow in the energetic favoured direction to form dendrites. The effective heat transfer rate of mold decides the morphology of cast structure i.e., dendritic, columnar, coarse, and fine structure. Further, the observation of micrographs through various researchers results in the presence of various secondary phases such as θ-(Al_2Cu), Mg_2Si, π-($Al_8Mg_3FeSi_6$), α-($Al_{15}(Mn, Fe)_3Si_2$), and β-(Al_5FeSi) as the function of temperature is shown in table 5.1[191]. The phase α-($Al_{15}(Mn, Fe)_3Si_2$) is a cubic crystal structure represented as a Chinese script, and the β-(Al_5FeSi) phase is a monoclinic crystal structure that appears as a needle-like structure[192]. The size of the β- phase depends on the amount of Fe content and solidification behaviour. The presence of the β-phase shows a detrimental effect on the mechanical properties of an alloy. The phase $CuAl_2$ is present in the blocky form or Al-$CuAl_2$ eutectic depending on the modifying alloying element. The shape of these phases has a significant effect on the alloy properties[193].

Table 5.1: Formation of phases at the interval of temperature[194]

Temp	Phases
610°C	α- Al dendrite
560°C	Al-Si eutectic, Increase the Cu content in the liquid
540°C	α-(Al_{15}(Mn, Fe)$_3Si_2$), Mg_2Si
525°C,	$CuAl_2$,β-(A_{l5}FeSi)
507°C	Eutectic CuA_{l2}- α- Al

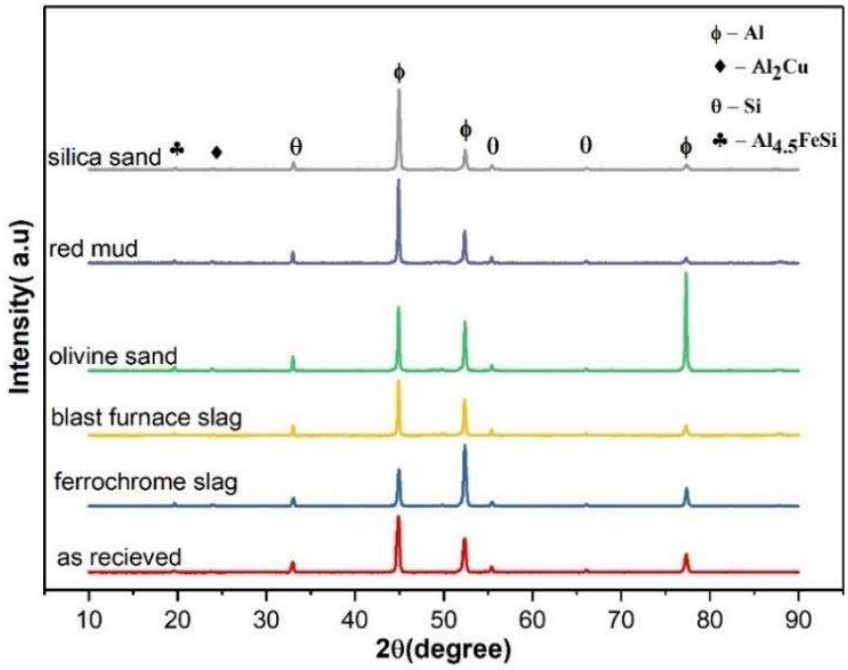

Figure 5.8: XRD of A319 alloy cast in a different mold

The main contributors to the formation of porosity in Al-Si-Cu alloys are (i) hydrogen concentration of the melt and (ii) Grain refiners and inclusion content and others. (iv) Solidification behaviour (iii) Secondary phases such as $CuAl_2$, β-(Al_5FeSi)[195]. Various researchers observed that the β-(Al_5FeSi) phase was the preferred site for the nucleation of pores and also tailored the pore size due to the low interfacial energy between gas and secondary phases[196].

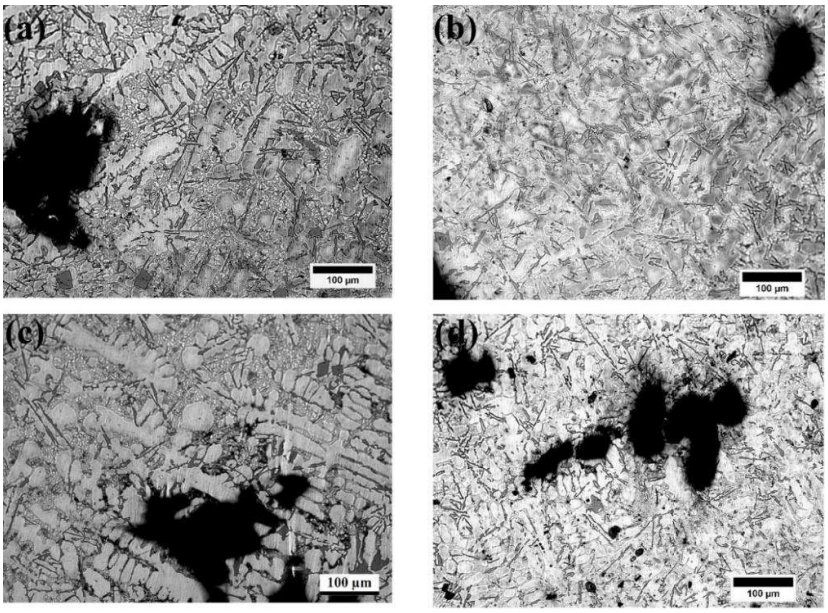

Figure 5.9: Porosity micrograph of A319 alloy cast in(a) silica sand mold (b) blast furnace slag mold (c) ferrochrome slag mold (d) red mud mold

The variation in porosity is shown in figure 5.9 with respect to the variation of the percentage of solid waste in a sand mold, which can alter the solidification rate. Pores are in the form of blow holes and shrinkage porosity. The shrinkage amount varies with the temperature, depending on the fraction of solids precipitated at given temperatures and the nature of the phases formed. Gas defects may result from the failure of the mold to exhaust air displaced by the liquid metal. Gas may have been dissolved during the melting or as a result of interaction b/w liquid metal surface or may results from reaction involving elements in solution. The factors affect the form & distribution of gas porosity. In some case gas can concentrate by the diffusion into the central region, the final defects apparat as blow holes, whilst in the other case dispensed porosity may be throughout the casting and in localized surface region due to high concentration of the gas resulting from metal-mold interaction. The solidification behaviour affects the pore size by affecting secondary dendritic arm spacing, which determines the threshold cell size and therefore the pore size. As cooling rates increase, the porosity and pore size of the alloy decrease [39].

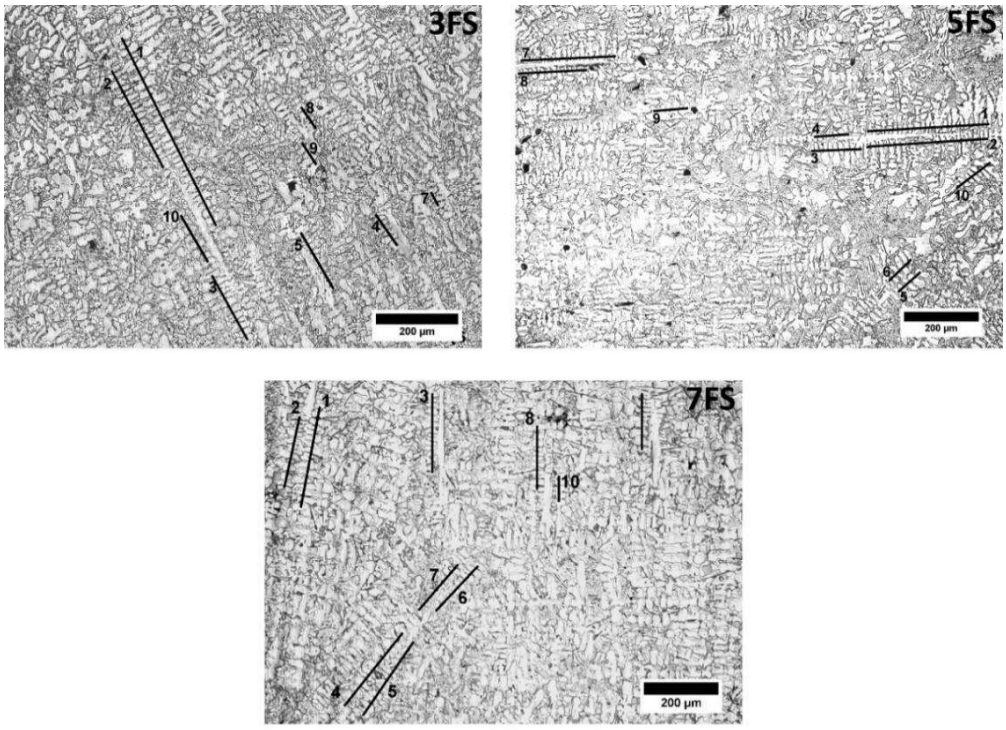

Figure 5.10: Dendritic microstructure of A319 cast in ferrochrome slag mold

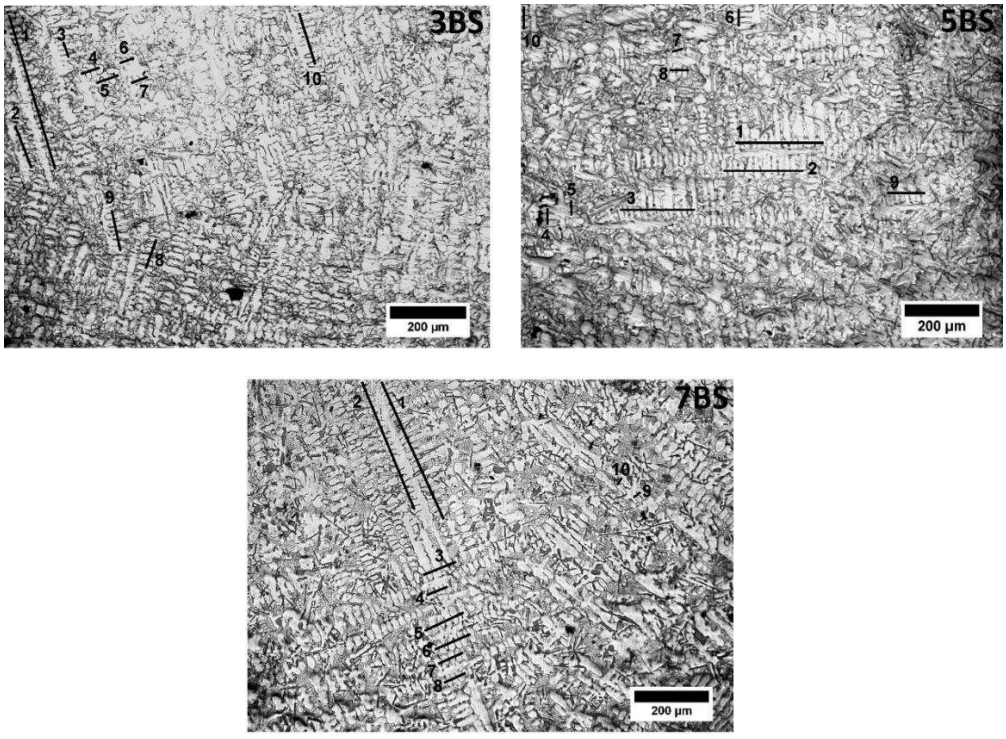

Figure 5.11: Dendritic microstructure of A319 cast in blast furnace slag mold

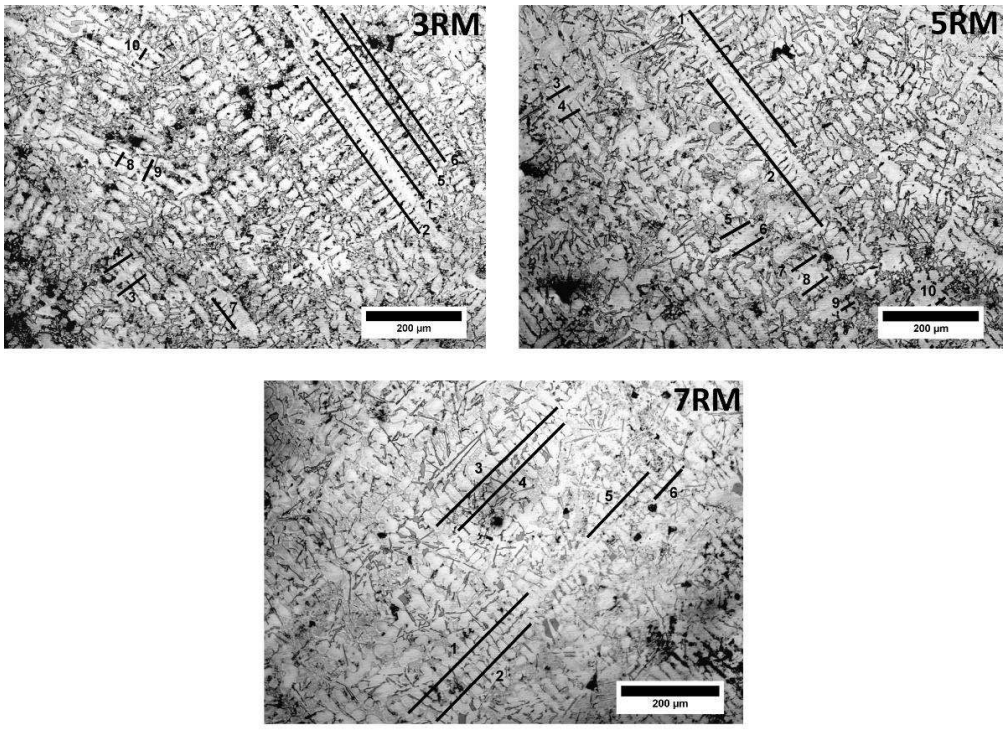

Figure 5.12: Dendritic microstructure of A319 cast in red mud mold

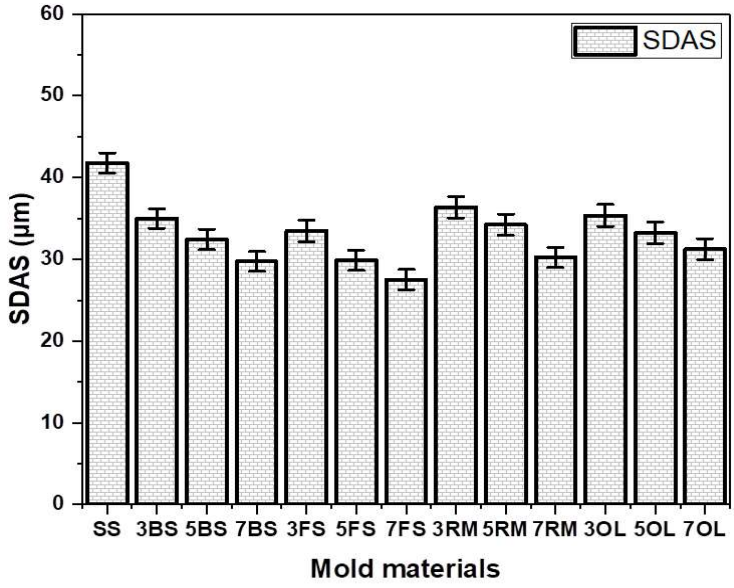

Figure 5.13: Secondary dendritic arm spacing (SDAS) of A319 alloy cast in a different mold

The morphology of microstructure depends on the SDAS (secondary dendritic arms spacing), which is the function of cooling rates, higher cooling rates result in a small SDAS

value. The space between the secondary dendrite was occupied by the eutectic or intermetallic phases present in the alloy. The measured value of SDAS of ferrochrome slag mold cast has a lower value as compared to the silica sand mold as shown in figure 5.13. Figure 5.10 – 5.12 shows the microstructure having a primary and secondary dendritic arm, the variation in the secondary dendritic was observed with the variation in the percentage of solid waste in the sand mold. The variation of solid waste enhanced the rate of rejection of heat from the mold to the atmosphere. A result of the high heat transfer rate was attributed to the faster cooling rate as well as the high solidification rate as shown in table 4.4. So, the variation in the solidification rate altered the morphology of the microstructure with the variation in the secondary dendritic arm spacing (SDAS). According to Figures 5.10 - 5.12, the average SDAS was found to be between 33 μm and 41 μm. The 7FS mold has the lowest SDAS value of 27 μm whereas the SS mold has 42μm, which states a 38% reduction in the size of SDAS. It is clear from the above figure that the slag mold causes a significant change in the microstructure with a decrease in SDAS. It was reported that the eutectic phase and intermetallic phase are also impacted by the cooling rate during solidification in addition to reducing the secondary dendritic arm spacings of the alpha-Al phase and hence improving the mechanical properties [197].

Due to constitutional undercooling, alloy solidification develops in dendrites with secondary and tertiary arms, influencing equilibrium solidification. During the solidification process, the solute is rejected ahead of the solidification front, which increases the concentration of solute in the front of the solid-liquid boundary and results in the variation of liquidus temperature. The disruption caused by the positive temperature gradient ahead of the solidification front results in the dendritic structure. The variation in the size of dendritic arm spacing is attributed to the solidification behaviour of an alloy[198]. Solute is partition into the liquid ahead of the solidification front. This causes a

corresponding variation in the liquidus temperature. There is however, a positive temperature gradient in the liquid, giving rise to a supercooled zone of liquid ahead of the interface. This is called constitutional supercooling because it is caused by composition changes. A small perturbation on the interface will be therefore expand into a supercooled liquid. This gives rise to dendrites. It follows that a supercooled zone only occurs when the liquidous temperature (T_L) gradient at the interface is larger than the temperature gradient as shown in figure 5.14.

$$\frac{\partial T_L}{\partial x} > \frac{\partial T}{\partial x} \tag{5.8}$$

The condition for constitutional supercooling criterion we need to consider mass flow only at the interface as per equation (5.8, 5.9 & 5.10).

$$\frac{dc_L}{dx} = \frac{-R}{D_L} c_L(1-K) \tag{5.9}$$

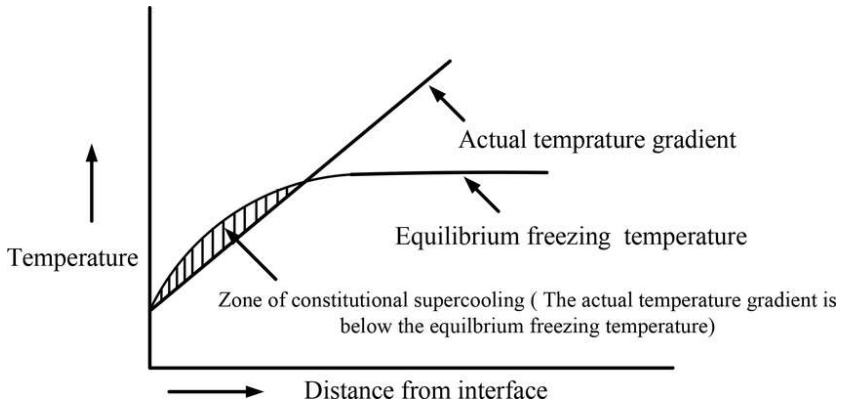

Figure 5.14: supercooling at the unstable interface

The slope of the curve of the equilibrium liquidus temperature T_L versus distance from the interface x, is related to the liquid composition C_L by the slope of the liquidus line m_L.

$$\frac{G_L}{R} > \frac{m_L c_o(1-K)}{KD_L} \tag{5.10}$$

Where x is the distance from interface, D_L is the diffusion coefficient of solute in the liquid, R is the rate of movement of interface, K is equilibrium partition ratio and C_o is the initial composition.

5.3.2 Tensile properties

Figure 5.15 shows the fracture pattern of the tensile test sample failure and observed that the fracture occurs along the gauge section of the sample. The presence of porosity in the sample surface facilitates the crack initiation to the failure of the sample. The fracture morphology states the brittle nature of failure due to having a large surface of facets with a low level of dimples takes place.

Figure 5.15: Fracture pattern of the tensile test sample of A319 alloy

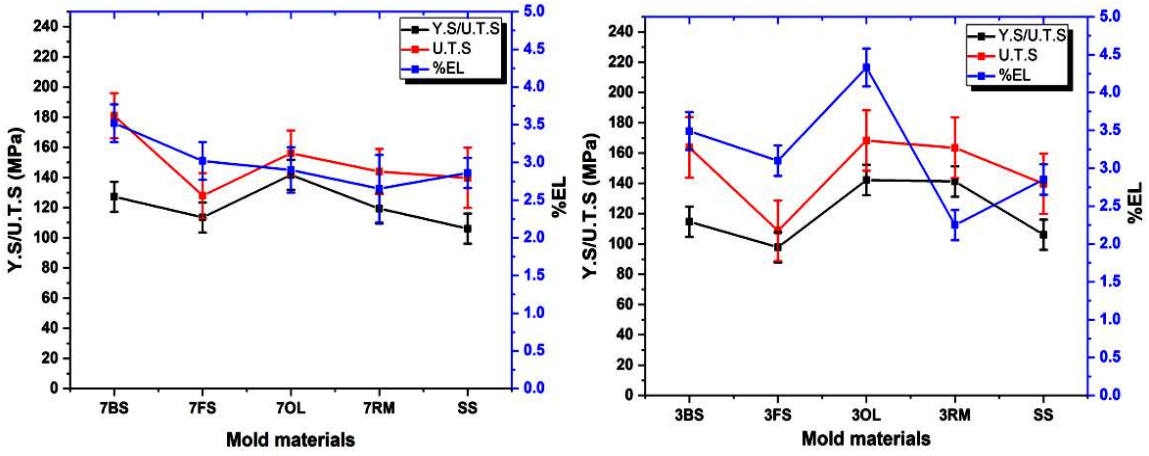

Figure 5.16: Tensile strength and elongation of A319 alloy cast in a different mold

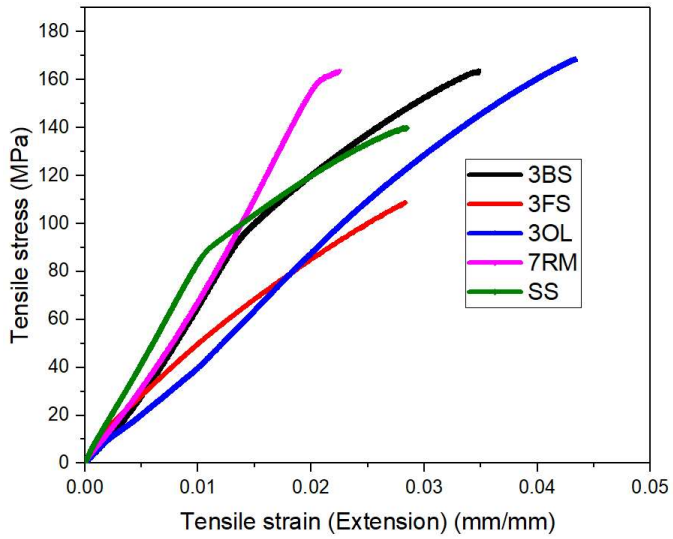

Figure 5.17: Tensile strength and elongation of A319 alloy cast in a different mold

Tensile properties such as ultimate tensile strength (UTS) and yield strength (YS) are improved with increased wt.% of slag in a sand mold as shown in figure 5.16. Ductility of the alloy defines on the basis of % elongation. The % elongation of cast A319 alloy varies from 2.68% - 3.50% with respect to different mold. The BS mold has ductility of 3.5% whereas ductility of red mold has 2.65. The area under curve of the stress strain defines the toughness of the cast, which mainly is the function of strength and ductility of the cast. From the figure 5.17 it observed that BS and OL mold cast has the area under the stress-strain was more as compared with the SS mold and hence toughness of the BS and OL mold cast was higher than the SS mold cast It is well known that the SDAS value has a substantial impact on the mechanical properties of the Al-Si casting alloys [199,200]. However, in the present investigation, the results of tensile properties are satisfactory with the reported data. Due to the variation in the distribution of porosity as shown in figure 5.9, a large dispersion of the tensile characteristics of samples with the same porosity level was observed. It was obvious that when the porosity level increases qualitatively, both EL and UTS drop. Furthermore, it was seen that the standard deviation of UTS rises monotonically as the porosity level rises, indicating worse consistency and dependability of samples with

greater porosity levels [201]. From the results of tensile properties, it was observed that slag mold cast alloy exhibits optimum YS and UTS values. The UTS and YS of alloy cast in 7BS mold increased by approximately 10% and 22% concerning sand mold.

i. *Evolution of tensile strength enhancement*

The strengthening mechanism of the above cast alloy may depend on the solidification behaviour that attributes to the secondary dendritic arm spacing, solute concentration, and volume fraction of phase concentration. The following strengthening mechanism such as grain boundary strengthening, solute strengthening, and strain hardening responsible due to the variation in the cooling rate that directly or indirectly affects SDAS. As the cooling rates increase leads to a decrease in the SDAS that promotes fine α-Al grain results in an enhancement in the tensile properties[202]. The percentage of mold material was only the variable that result in the variation of SDAS. Due to the complexity of the as-cast structure, it was difficult to estimate the phenomena of strengthening an alloy.

ii. *Fractograph*

The result of tensile strength shows that the variation in the % of solid waste in the sand mold was not leading to elongation changes in the alloy, which was reflected in the fractograph having a similar mode of failure takes place. Analysis of the fracture mechanism and causes under tensile loading was the goal of the SEM fractograph of the tensile sample. The SEM fractograph of Al-Si alloy cast in various molds is displayed in Figure 5.17. When the fractograph morphology was initially seen, the corresponding tensile loading situations all showed comparable features. The cleavage fracture with flat facets is represented by the notations A and B. An edge, such as the ridge shown by the arrow, is divided into two aspects shown in Figure 5.18.

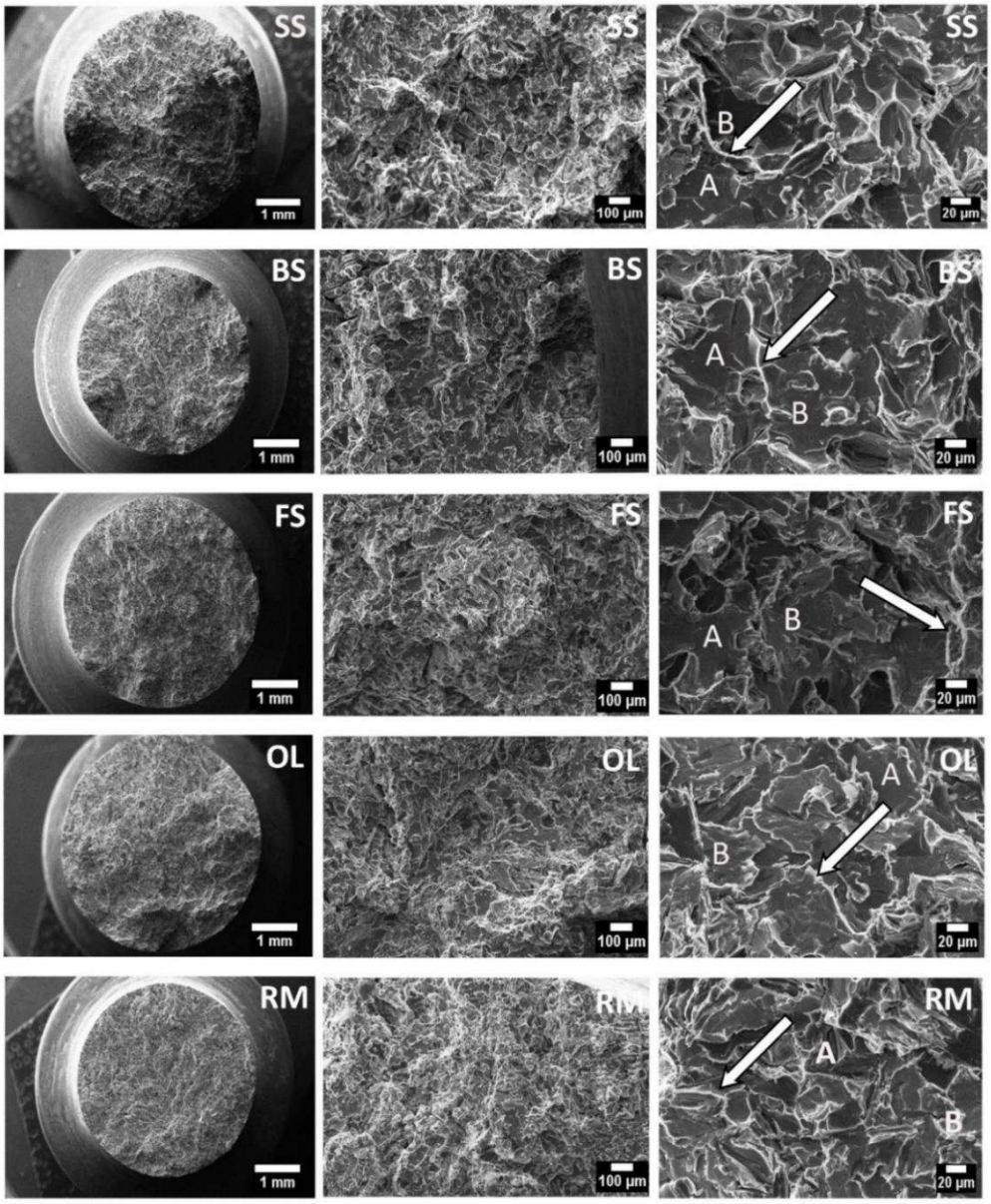

Figure 5.18: Fractograph of A319 alloy cast in a 70% slag-sand mold

The Si phase is separated from the aluminium matrix is what caused the ridges to form. A brittle fracture can be seen on the fractograph with several facets. Si-particles cracking and fracturing, which only affected a piece of the Al matrix, produced a typical cleavage-fracture mode. It was discovered that the entrapped shrinkage pores are randomly distributed throughout the distorted Al matrix and eutectic Si particles at low magnification. es [203]. According to the microstructure, the phase present in this alloy was intermetallic,

Al-Si eutectic, and a few primary blocky Si. The Si platelets were thought to extend sequentially in the Al-Si eutectic. Because of this, the fracture in the eutectic Al-Si alloy might easily spread along the boundary between the Si platelets and the Al matrix. We were unable to detect the evident ductile dimples as a result of the fracture appearance. The applied tensile stress causes the Al matrix around the Si platelet to deform severely, which causes Al-Si debonding and the creation of micro voids at the Al-Si interface. These tiny cracks may interact with one another and develop at the Al-Si contact under strain. The crack's existence causes a significant stress concentration at its tip along the Al-Si interface, which might lead to both the fracture of the harder Si platelet and the formation of further cracks inside the Al matrix. The matrix acts as a medium for the crack to spread. Therefore, the fracture spreads along the Al-Si contact by the matrix microcracks coalescing [204].

5.3.3 Hardness

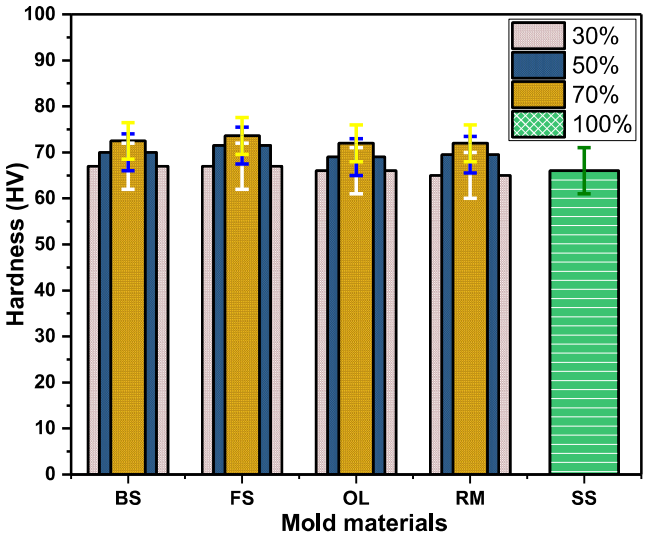

Figure 5.19: Hardness of A319 alloy cast in a different mold

Figure 5.19 shows the hardness of the A319 alloy cast in a different mold. It can be observed that the hardness increased with an increase in solid waste content in silica sand mold. The FS mold casting shows the optimum hardness value as compared with the other mold. The higher the solid waste content in silica sand mold shows the higher hardness

whereas 30% of solid waste in silica sand mold shows approximately similar trends to the hardness of an alloy cast in silica sand mold. Solid waste content in sand mold can accelerate the transfer of heat from mold to the surrounding which enhanced the cooling rates of casting. The higher cooling rate of casting resulted in higher hardness[205]. The higher cooling rates result in a decrease in the size of a micro constituent, Si particle, secondary dendritic arm spacing, etc as compared with the low cooling rates[206].

5.3.4 Density and Porosity

The cast structure of Al-Si alloy mainly consists of the most common defect i.e., porosity. The main reason behind the formation of porosity was solidification and casting parameters. Solidification involves can be shrinkage, absorption of hydrogen gas, bad feeding of liquid metals[207,208], and casting parameters such as heat dissipation, gas entrapment, and pouring process[209].

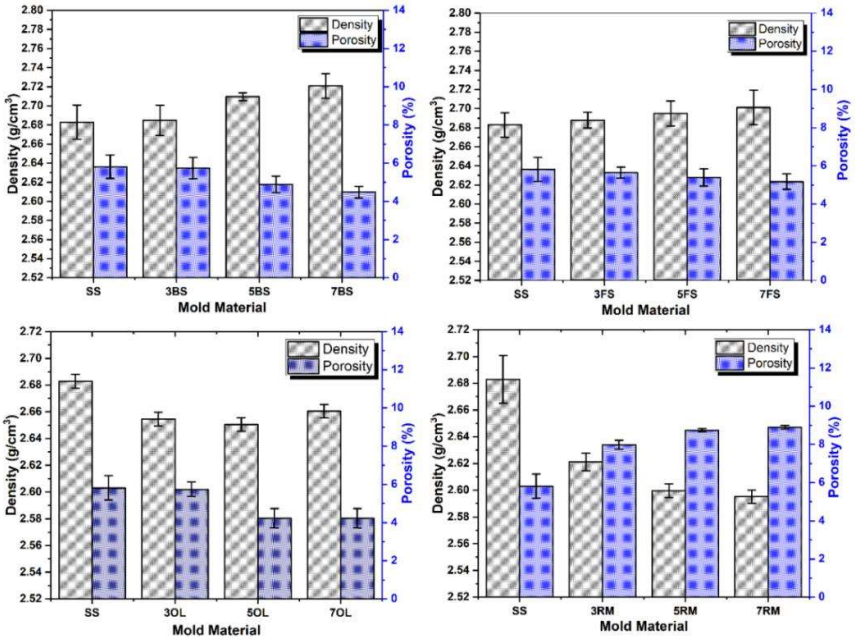

Figure 5.20(a): Density and porosity of A319 alloy at location 1 cast in a different mold

The density and porosity of the A319 alloy cast in the different molds are shown in figure 5.20. The density of the cast was measured at two different locations along the cross-section

i.e. locations 1 and 2 shown in figure 5.20(a) and 5.20(b) respectively. From the result, it was observed that the density of the sample varied along the cross-section and observed that at location 1 the density of A319 alloy cast in different molds are approximately the same but the density of red mud mold cast was low as compared with the rest casting.

The results showed that the cast of the 7BS, 7FS, and 7OL mold has high density and minimum porosity as compared with the rest slag and SS mold while a cast of the RM mold showed a higher porosity level. The low porosity level of a cast in 70% slag-sand mold might be due to the better particle size distribution which provided minimum entrapment of gas or a good permeability level that allows hot gases to escape as shown in figure 5.19(a). Also, from SDAS the solidification rate was higher in BS and FS mold as compared with RM mold due to having higher heat dissipation from mold to the surrounding, which attributed that BS and FS mold has low porosity level as compared with the RM mold.

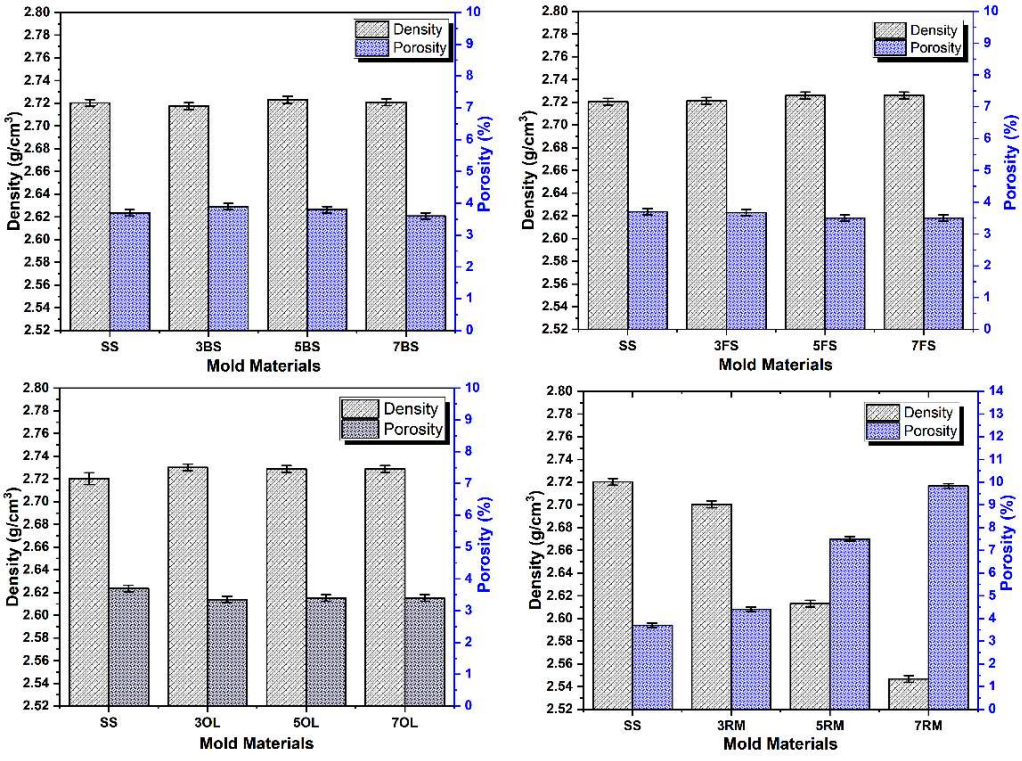

Figure 5.20 (b): Density and porosity of A319 alloy at location 2 cast in a different mold

5.3.5 Wear rate

Generally, the volume of worn materials or wear rates is directly proportional to the load or force, sliding distance, and inversely proportional to the hardness according to Archard's law[210]. It is known from the study that under constant frequency or sliding distance the wear rate is directly proportional to the applied load and the solidification rate is inversely proportional to the wear rates. Solidification rates change the coarse dendritic to fine dendritic structure in the case of slag mold as compared to sand mold resulting in high wear resistance. The wear rate of Al-Si alloy was calculated using the weight-loss method. The weight of the sample before and after the wear test was measured to estimate the weight loss. Each test was performed three times for experimental error estimation and the Wear rate was calculated as weight loss per unit of sliding distance (mg/km). The wear rate versus applied load with the variation in the load and frequency was shown in figure 5.20. From figure 5.20 the wear rate of alloy increase with an increase in the load and frequency and also it was observed that the wear rate of alloy cast in BS mold and FS mold are less as compared to the SS mold and red mud mold. The hardness of an alloy resists the penetration of indentation, which hindered the ploughing of the surface and hence improves the wear resistance. Figure 5.21 (a) and (b) show the wear rate of A319 alloy against the BS mold, FS mold, OL mold, and RM mold and compared it with the silica sand mold at different loads and frequencies. It was observed that an increase in load (5N-15N) and frequency (5Hz-15Hz) increases the wear rate and approximately equal rate of increment in different mold casting, which indicates a similar mode of wear occurs. At a high load, the Porosity of an alloy facilitates the fracture of the pore edge, which attribute to the propagation of the crack, delamination, and ploughing action and hence deteriorate the wear resistance of an alloy[211,212]. The result shows that the casting in RM mold was having a higher wear rate, which might be due to the higher porosity level as compared

with the rest mold. At high load and high frequencies, the wear rate of an alloy cast in7BS, 7FS, 7OL, 7RM, and SS mold are 7.7, 7.7, 7.7, 7.9, and 7.9 mg/Km respectively but at low load & frequency wear rate of alloy cast in 7BS, 7FS, 7PL, 7RM & SS are 3.85, 2.51, 3.75, 5.41 & 5, which signify that the cast in BS mold and FS mold enhanced wear resistance of cast alloy at low load and frequency.

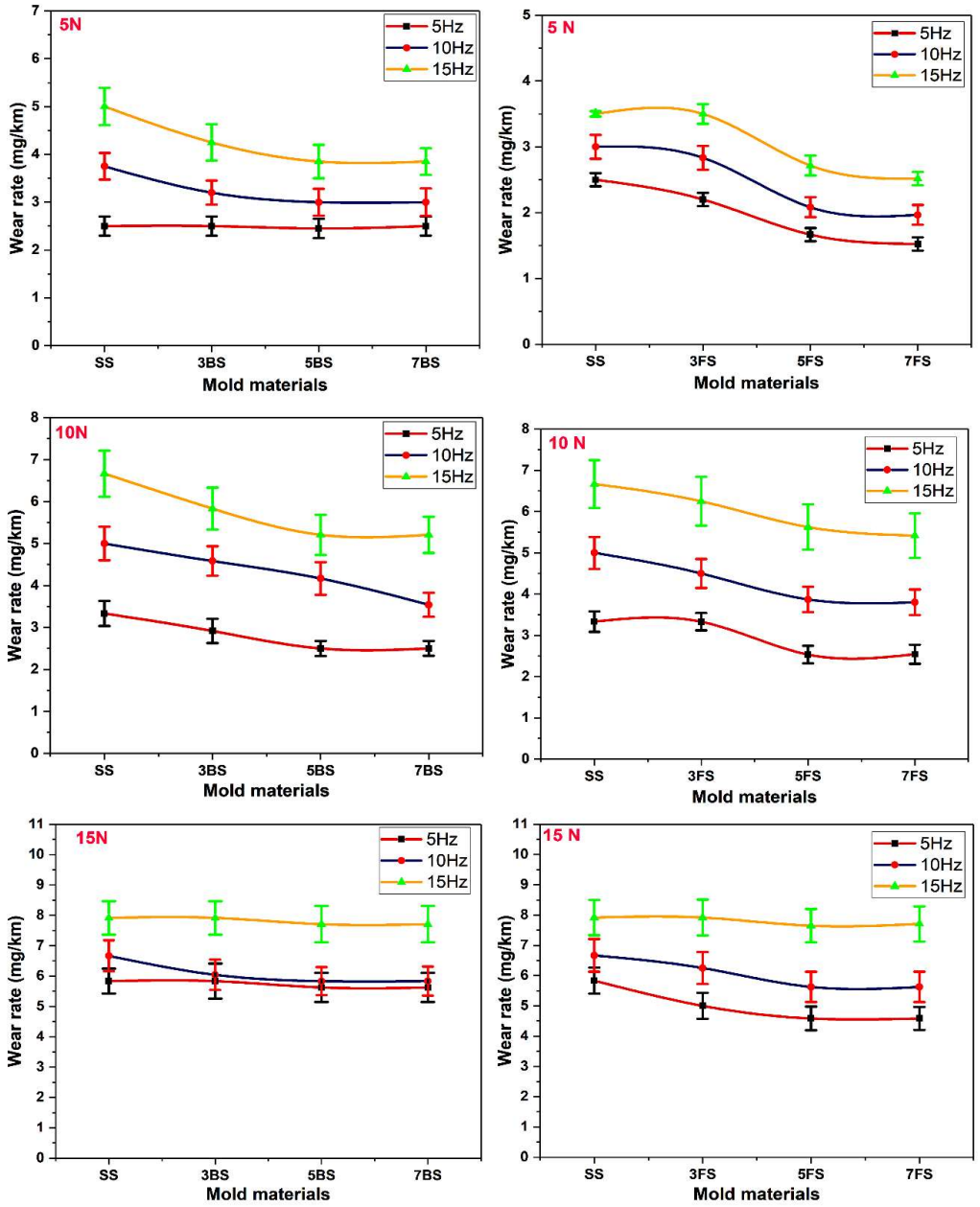

Figure 5.21 (a): Wear rate of A319 alloy against mold materials at different loads and frequency

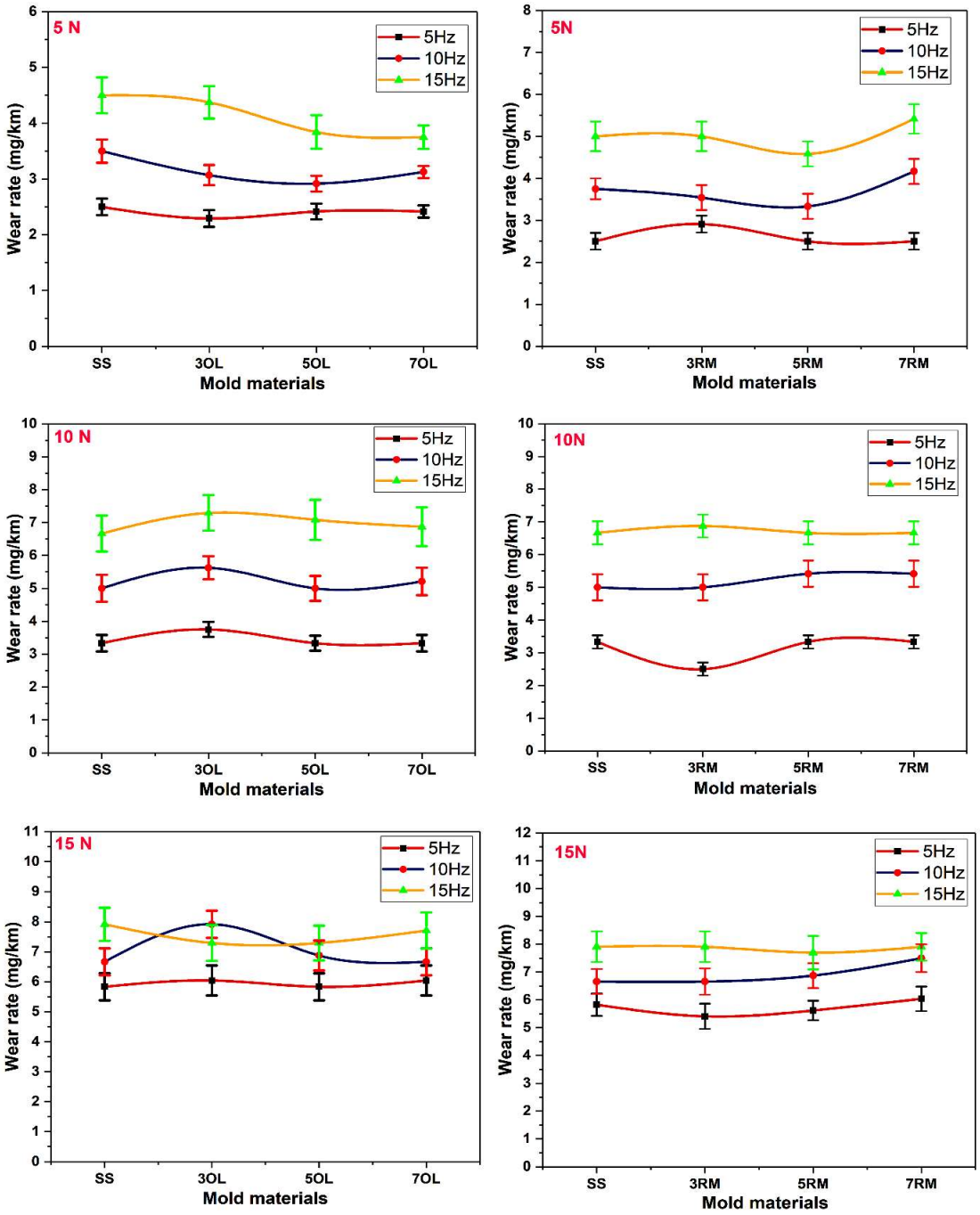

Figure 5.21(b): Wear rate of A319 alloy against mold materials at different loads and frequencies

5.3.6 Coefficient of friction (COF)

The coefficient of friction (COF) was used for the measurement of the amount of frictional force existing between two surfaces during the reciprocating wear of a sample as shown in figure 5.22. It is a dimensionless number and was defined as the ratio of frictional force to the normal force. It depends on the nature of the material and surface roughness. A wear test was conducted using a reciprocating ball on a disc to investigate the effect of load and frequency on the hypoeutectic alloy cast in a different mold. The variation in coefficient of friction may be due to the plastic deformation of an alloy at high load, at high load surface become smooth and decreases the coefficient of friction whereas the COF increases may due to the extensive deformation of the subsurface. The maximum value of COF i.e. 0.74 was observed in red mud mold at 10N-15Hz as shown in figure 5.22.

Interestingly, it was observed from figure 5.22 that the average value of the coefficient of friction was about the same in all casting concerning variation in the load and frequency, the value lying between 0.45 to 0.55, Which accounts for the same phenomenon or similar wear resistance of the cast.

It can be observed from Fig. 5.22 that the coefficient of friction (COF) was lowest for SS mold and slag mold in the case of 5 Hz frequency at all tested loads. This may be due to the rolling of generated wear debris in the confined area. Reciprocating sliding is confined area sliding and there was not any dominant lip formation in reciprocating sliding in contrast to what was observed in unidirectional sliding.

Due to the lower hardness of alloy from SS mold, asperities penetrated deeper. Thus, the generated debris combined to form a relatively bigger lump that rolled in between the alloy and counter surface, which decreased the coefficient of friction. In the case of 10 Hz and 15 Hz frequencies, it was very difficult to generalize the friction response of Al-Si alloy

concerning mold material. This may be due to the increased frictional energy with an increase in frequency. Thus, the wear debris lump which was formed for SS mold and slag mold at 5 Hz frequency was difficult to form at 10 Hz and 15 Hz frequencies due to increased heat which plasticized the debris material. The scanning electron microscopy (SEM) micrograph of worn surface A319 alloy at 15N load and 15 Hz frequency as shown in figure 5.23 reveals the delamination, craters, and surface damage as an important mechanism for the wear or the loss of material, states the mild or severe wear takes place. In figure 5.23 (a &b) many parallel tracks were observed which indicate the combination of adhesive and abrasive wear mechanism takes place at 15N and 15Hz frequency which is also known as the ploughing of the surface.

Ploughing results, the widening, and deepening of wear track due to plastic flow of materials and groves are also observed as the displacement of aluminum takes place and between the grove, a ridge also appears, as the continuous process of reciprocating steel ball flattened the ridges and also a detachment of surface takes place. it was observed that three-body abrasive wear mechanisms are due to the presence of particles on the wear track, these particles on the wear track can be due to the detachment of the surface of the alloy or the steel ball. From figure 5.23 (b), due to fracture of the surface, it was observed severe wear on the surface, these fracture starts from the pores present on the surface as each pore connect and form a network. Figure 5.24 show the XRD of wear debris and confirm the oxidative nature of wear.

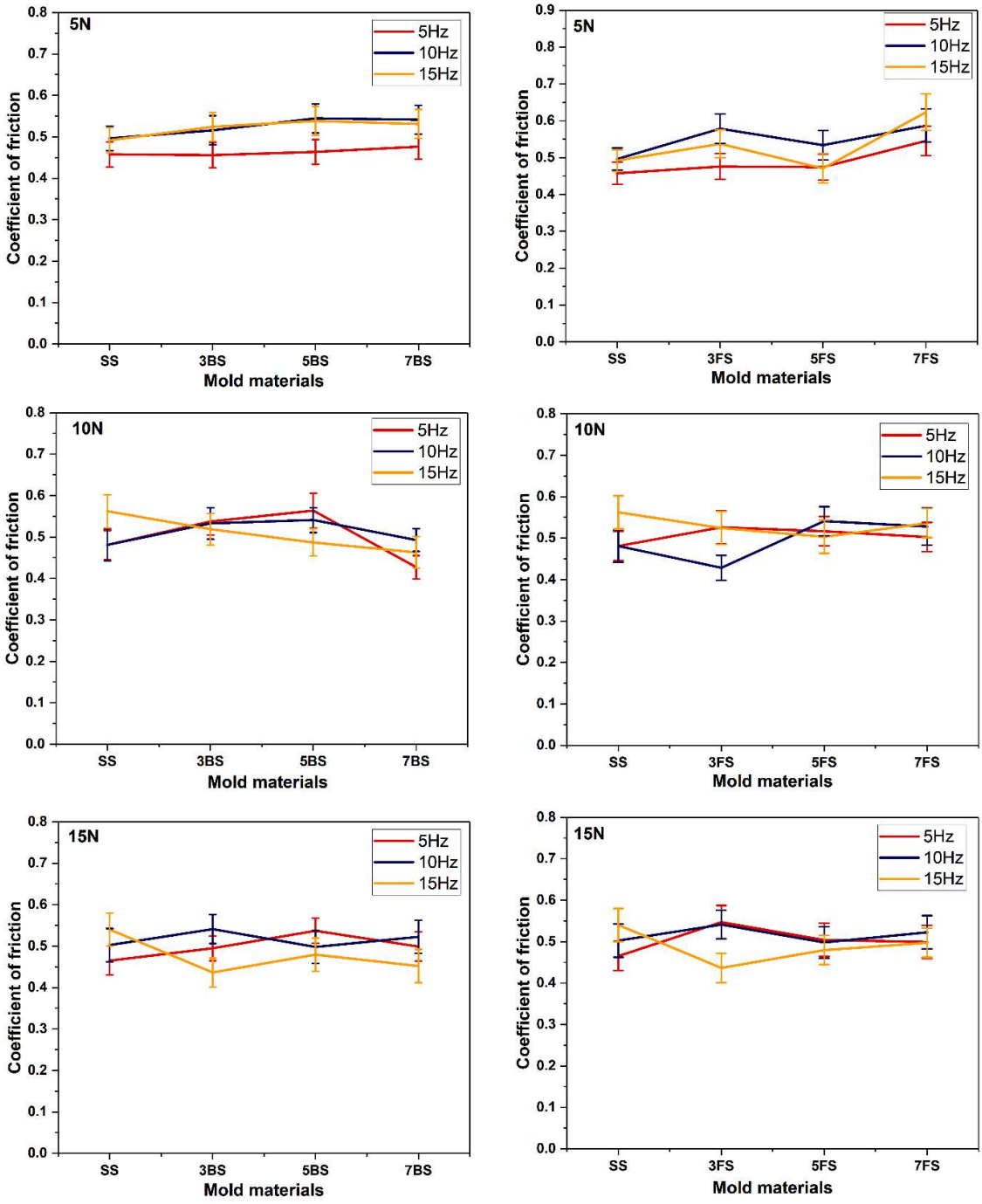

Figure 5.22(a): Coefficient of friction (COF) of A319 alloy against mold materials at different loads and frequencies

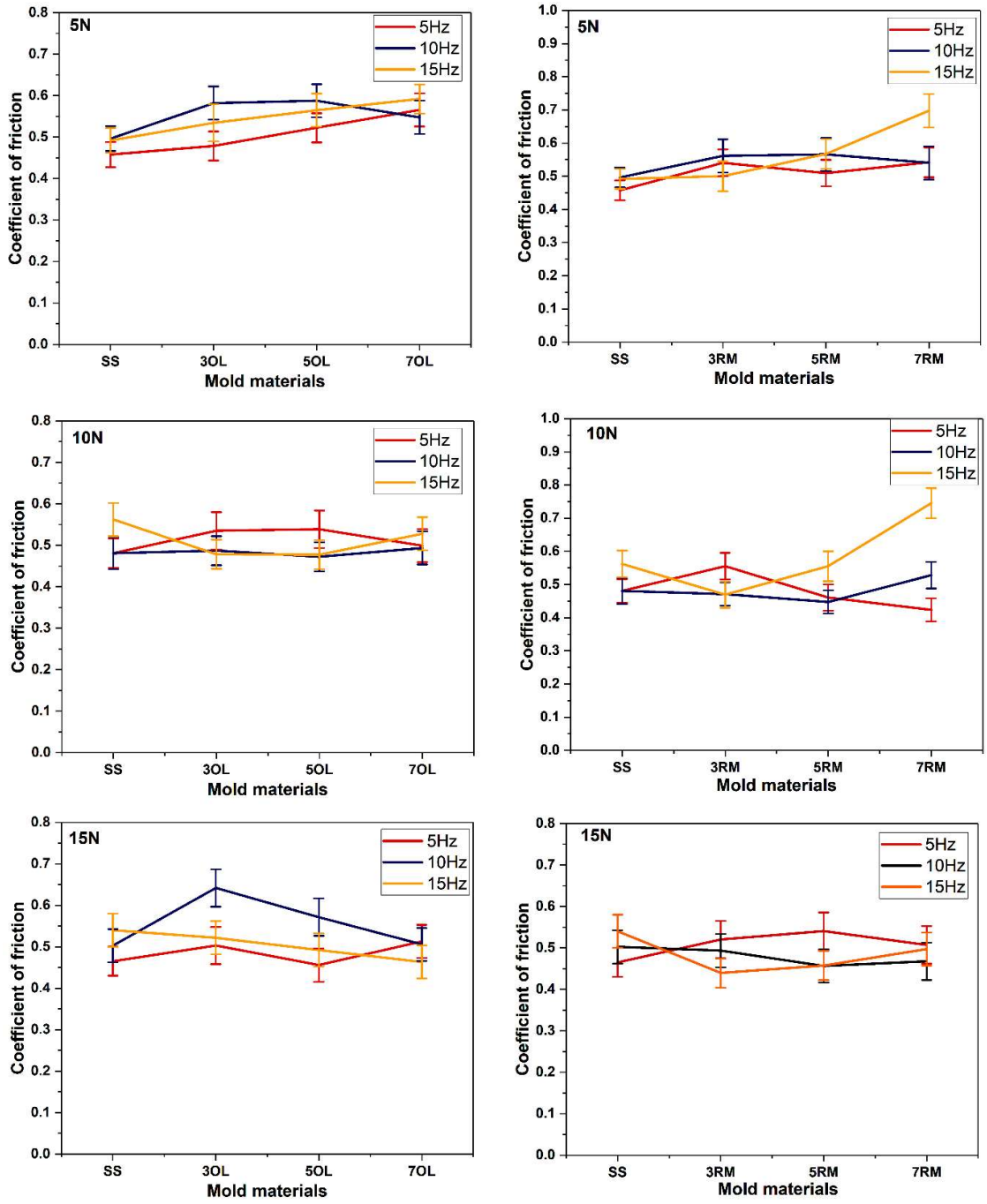

Figure 5.22(b): Coefficient of friction (COF) of A319 alloy against mold materials at different loads and frequencies

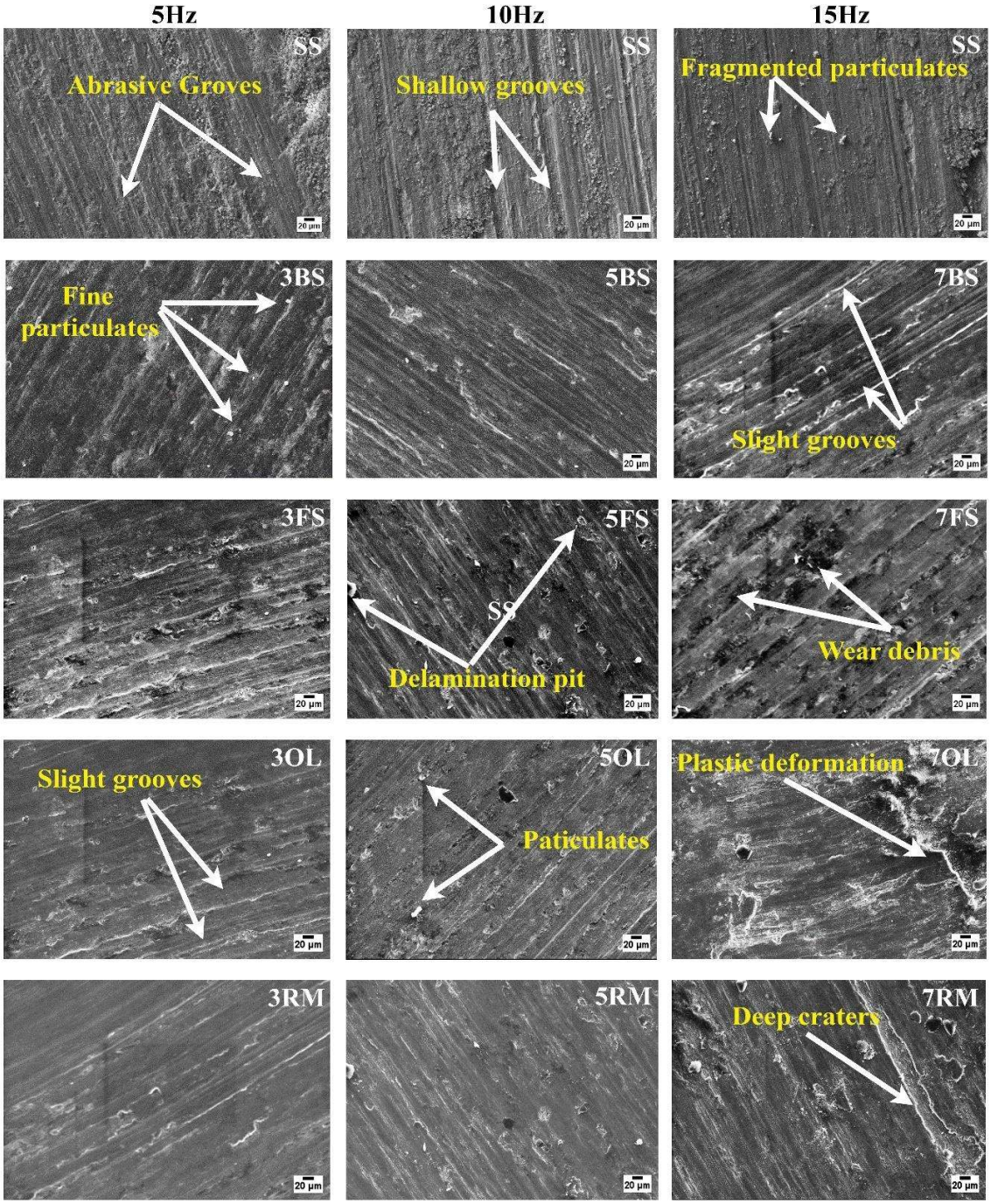

Figure 5.23(a): Worn surface morphology of A319 alloy cast in a different mold at 05N load with variation in the frequency 5Hz-15Hz

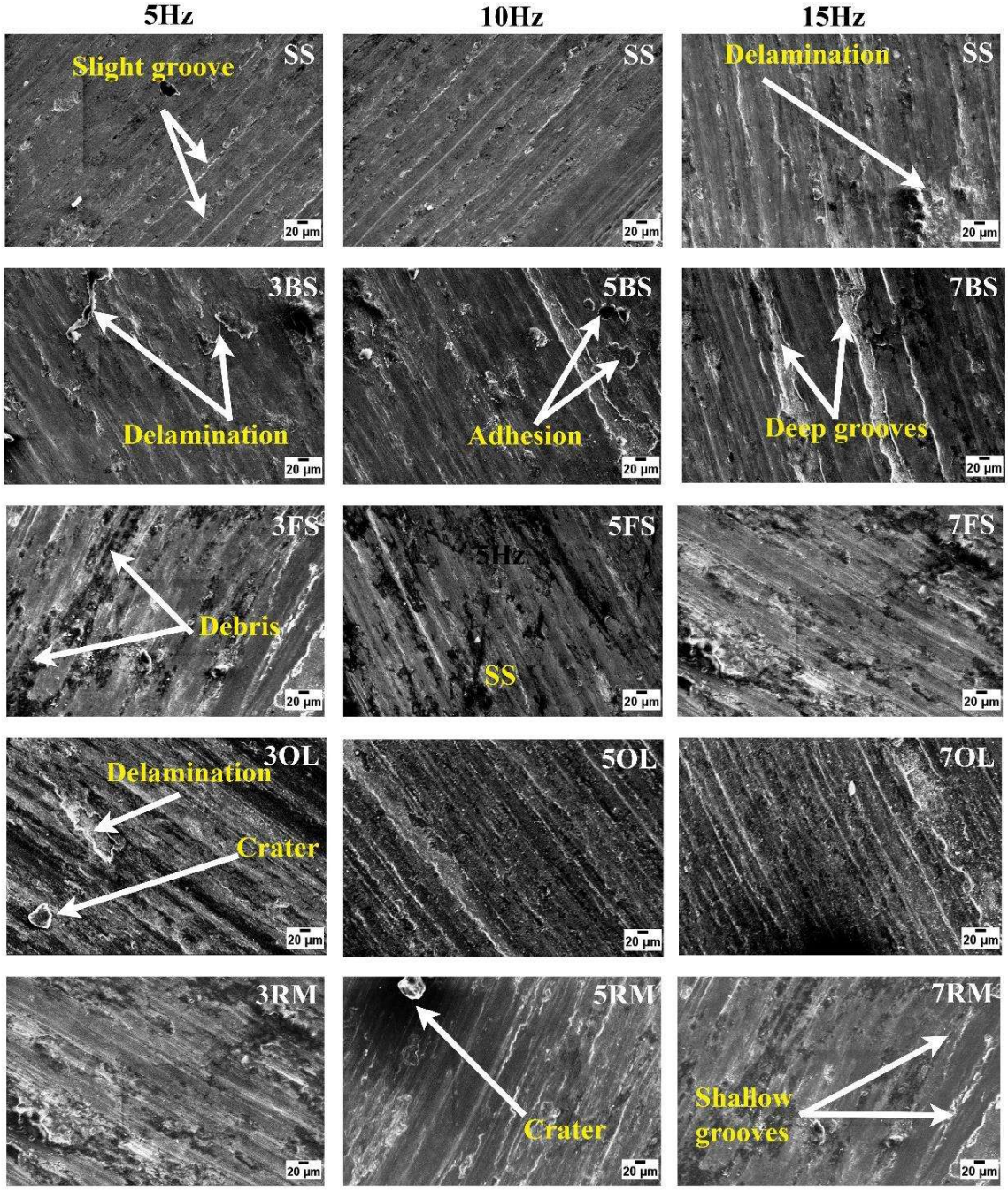

Figure 5.23(b): Worn surface morphology of A319 alloy cast in a different mold at 15N load with variation in the frequency 5Hz-15Hz

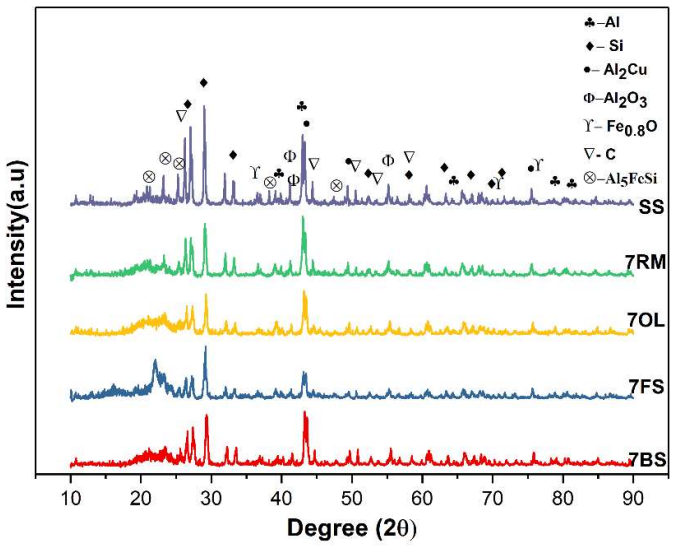

Figure 5.24: XRD of wear debris

5.4 CONCLUSIONS

- The microstructure of A319 consists of a white α- Al dendrites network, dark grey silicon particles, and eutectic Al-Si segregated into the inter-dendritic region, Al_2Cu phase.
- XRD confirms the presence of the Al_2Cu phase and Al-Fe-Si phase.
- The 7FS mold has the lowest SDAS value of 27 µm whereas the SS mold has 42µm, which states a 38% reduction in the size of SDAS.
- The density of as cast A319 alloy in BS, FS, and OL mold has approximately similar values but 7RM mold increases the approximately 50% in porosity of an alloy as compared with SS mold.
- The yield strength of A319 alloy cast in 70% blast furnace slag mold, 70% ferrochrome slag mold, & 70% olivine sand mold was 127.2 MPa, 113.5MPa, 141.74MPa respectively and ultimate tensile strengths are 180.94 MPa, 127MPa, 156MPa respectively.

- For the constant load and frequency wear rate of cast A319 alloy decreases with an increase in wt.% of solid waste except in sand mold with respect to sand mold.
- The wear rate of A319 alloy increases with an increase in applied load and frequency of cast in slag and sand mold.
- The coefficient of friction of A319 shows a fluctuating tendency of increasing with time at low load and frequency but at high load and frequency, it observed a decreasing tendency.
- Worn surface morphology reveals reduced delamination, metal flow, and shallow ploughing in 7BS and 7FS mold cast at load and frequency.
- Worn surface and debris analysis show mild oxidative wear at high load and frequency as well as sever-metallic wear.